

Time-reversal symmetry breaking in charge density wave of CsV_3Sb_5 detected by polar Kerr effect

Yajian Hu^{1*}, Soichiro Yamane¹, Giordano Mattoni^{1,2}, Kanae Yada¹, Keito Obata¹, Yongkai Li^{3,4,5}, Yugui Yao^{3,4}, Zhiwei Wang^{3,4,5}, Jingyuan Wang⁶, Camron Farhang⁶, Jing Xia⁶, Yoshiteru Maeno^{1,2}, Shingo Yonezawa^{1†}

¹*Department of Physics, Graduate School of Science, Kyoto University, Kyoto 606-8502, Japan*

²*Toyota Riken-Kyoto University Research Center (TRiKUC), Kyoto University, Kyoto 606-8501, Japan*

³*Centre for Quantum Physics, Key Laboratory of Advanced Optoelectronic Quantum Architecture and Measurement (MOE), School of Physics, Beijing Institute of Technology, Beijing 100081, P. R. China*

⁴*Beijing Key Lab of Nanophotonics and Ultrafine Optoelectronic Systems, Beijing Institute of Technology, Beijing 100081, P. R. China*

⁵*Material Science Center, Yangtze Delta Region Academy of Beijing Institute of Technology, Jiaxing 314011, P. R. China*

⁶*Department of Physics and Astronomy, University of California, Irvine, California 92697, USA*

*e-mail: hu.yajian.78e@st.kyoto-u.ac.jp †e-mail: yonezawa@scphys.kyoto-u.ac.jp

Dated: August 18, 2022

The Kagome lattice exhibits rich quantum phenomena owing to its unique geometric properties. Appealing realizations are the Kagome metals AV_3Sb_5 ($A = \text{K, Rb, Cs}$), where unconventional charge density wave (CDW) is intertwined with superconductivity and non-trivial band topology. Several experiments suggest that this CDW is a rare occurrence of chiral CDW characterized by orbital loop current. However, key evidences of loop current, sponta-

neous time-reversal symmetry-breaking (TRSB) and the coupling of its order parameter with the magnetic field remain elusive. Here, we investigate the CDW in CsV_3Sb_5 by magneto-optic polar Kerr effect with sub-microradian resolution. Under magnetic field, we observed a jump of the Kerr angle at the CDW transition. This jump is magnetic-field switchable and scales with field, indicating magneto–chirality coupling related to non-trivial band topology. At zero field, we found non-zero and field-trainable Kerr angle below T_{CDW} , signaling spontaneous TRSB. Our results provide a crucial step to unveil quantum phenomena in correlated Kagome materials.

The Kagome lattice has gained the spotlight over decades because of its rich ground states owing to its intriguing band structure. The nearest-neighbor tight-binding model of a two-dimensional (2D) Kagome net depicts presence of a flat band, Dirac cones, and van Hove singularities (vHSs). The flat band with localized electrons gives rise to strongly correlated phenomena, while the Dirac cones assist systems to become topological insulators or Weyl semimetals^{1,2}. The vHSs, showing divergent density of states, can lead to electronic instability such as spin-density wave and charge-density wave (CDW).

The Kagome metals $AV_3\text{Sb}_5$ ($A = \text{K, Rb, Cs}$) have attracted tremendous interest recently³. Crystallographically, vanadium atoms form an ideal 2D Kagome net at ambient temperature (Fig. 1a, b). In the band structure, traces of the flat band, Dirac cones, and vHSs expected for a 2D Kagome net all appear⁴. Both the Dirac cone and vHSs are located close to the Fermi level, promoting the topological and strongly correlated phenomena. $AV_3\text{Sb}_5$ compounds display CDW

order and superconductivity³⁻⁶. Moreover, giant anomalous Hall effect (AHE) is reported to occur concurrently with the CDW transition in KV_3Sb_5 ⁷ and CsV_3Sb_5 ⁸. Angle-resolved photoemission spectroscopy (ARPES)⁹⁻¹² and X-ray scattering¹³ experiments show a strongly momentum-dependent CDW gap and indicate that the CDW transition is triggered by Fermi surface nesting dominated by vHSs. In the context of lattice distortions in the CDW state, the acoustic phonon anomaly is absent¹³ while the hardening of an optical phonon mode is reported¹⁴. These results establish the unconventional nature of the CDW in the normal-state and it can profoundly influence the superconducting state, which also exhibits intriguing features¹⁵⁻²⁰. Thus, AV_3Sb_5 provide a versatile platform to investigate the interplay between novel band topology, CDW and superconductivity in the Kagome lattice.

A critical issue of the CDW in AV_3Sb_5 concerns the accompanied symmetry breakings. In scanning tunnelling microscopy (STM) studies, three-dimensional $2 \times 2 \times 2$ or $2 \times 2 \times 4$ charge modulations have been mapped out^{19,21}. Interestingly, clockwise or counterclockwise intensity modulation of putatively identical superlattice peaks exist and can be flipped by magnetic field, as reported for all members of the AV_3Sb_5 family²²⁻²⁴. These results raise the possibility of time-reversal symmetry breaking (TRSB) although the long-range magnetic order is absent³. Zero-field muon spin relaxation (μ SR) on KV_3Sb_5 and CsV_3Sb_5 show enhanced relaxation rates in the CDW states, supporting the TRSB^{18,25,26}. On the other hand, an additional C_6 rotation symmetry breaking is found at a lower temperature in the CDW state and the electronic ground state is proposed to be nematic^{22,24,27-31}. Theoretically, the TRSB and rotation symmetry breaking can be well-explained by orbital loop currents and chiral flux induced as a consequence of order parameters

with non-zero imaginary component. Such an unconventional CDW state is now called chiral CDW.^{32–35} However, several experiments report the absence of TRSB in the CDW phase^{27,36–38}, and theories propose the charge bond order with real order parameters^{39,40}. We comment that the charge distribution in the CDW state can have a structural chirality⁴⁰, which should not be confused with the chirality and TRSB due to loop current. For a thorough understanding of the CDW in AV_3Sb_5 , new probes of TRSB are crucial.

Here, we performed high resolution magneto-optic Kerr effect (MOKE) measurements to investigate the CDW in CsV_3Sb_5 , a canonical member of the AV_3Sb_5 family. We measured the polar Kerr effect (PKE) using a zero-loop Sagnac interferometer. Different from the ordinary optical setup, PKE measured with our setup is only sensitive to TRSB of the system⁴¹. This technique has been used for studying novel TRSB phases in quantum materials, for instance, the chiral SC of Sr_2RuO_4 ⁴² and uranium-based superconductors⁴³, and the chiral charge order in the high- T_c cuprates⁴⁴. Using a newly-built all-fiber Sagnac interferometer, we measured polar Kerr angle θ_K at low temperature with sub-microradian resolution, with and without magnetic field. Under magnetic field, the polar Kerr angle jump $\Delta\theta_K$ at the CDW transition is almost linear in field and changes sign with opposite field direction. We demonstrate that this strong coupling to magnetic field is related to non-trivial band topology. At zero field, non-zero θ_K has been detected below T_{CDW} . This spontaneous θ_K is switchable by out-of-plane magnetic fields applied while cooling across the CDW transition, implying spontaneous TRSB in CsV_3Sb_5 . Our results can be well-interpreted by a magnetic-field switchable loop-current order in the chiral CDW.

Results

Crystal characterization and CDW transition in reflectivity. Before optical measurements, the samples were characterized by Laue diffraction and magnetic susceptibility. The Laue diffraction image shown in Fig. 1c displays clear spots, consistent with the hexagonal ($P6/mmm$) crystal structure at room temperature and indicating high crystal quality without significant stacking faults. The magnetic susceptibility shows sharp transitions at ~ 94 K and ~ 2.9 K, corresponding to the CDW and the superconducting transitions, respectively (see Supplementary Fig. S1). These data are consistent with previous reports^{3,4} and demonstrate that the samples are well single-crystalline.

In our PKE experiments, we used a broadband light source with center wavelength of ~ 1550 nm, and the phase of the light is modulated by the phase modulator with the frequency $\omega/2\pi \sim 3.848$ MHz. We detect the first and second harmonic components of the reflected signal from a photo detector⁴². The second harmonic signal $V_{2\omega}$ is proportional to the reflectivity of the sample, while the ratio between the first harmonic signal $V_{1\omega}$ to $V_{2\omega}$ gives the polar Kerr angle $\theta_K \approx 0.271V_{1\omega}/V_{2\omega}$ (See Methods). Figure 1d displays the temperature dependence of $V_{2\omega}$ for several selected magnetic fields between 0 T and 10 T. Upon cooling, the reflectivity jumps and increases below ~ 93 K. Because of the gap opening at the CDW transition, the spectral weight of low-energy optical conductivity shifts to higher energy ranges. This leads to the increase in the reflectivity at our wavelength, ~ 1550 nm (0.8 eV), as observed by the optical spectroscopy^{45,46}. From the temperature derivative of $V_{2\omega}$ ⁴⁷, we extract the transition temperature T_{CDW} at different magnetic fields and plot it in the inset of Fig. 1d. Among the three samples that we have measured,

T_{CDW} is located within the range 93 ± 0.5 K, and remains independent of the external field up to 10 T.

Polar Kerr angle measurements under magnetic field. We first present the polar Kerr angle θ_{K} under magnetic field. Because of the Faraday effect of the lens, there is a background signal contributing to the measured θ_{K} . In order to examine the signal from the sample across T_{CDW} , we use the measured θ_{K} of a Nb metal sheet to subtract the background signal $\theta_{\text{K}}^{\text{bg}}$ (see Supplementary Fig. S2). Figure 2a shows extracted sample signal $\theta_{\text{K}}^{\text{sample}} = \theta_{\text{K}} - \theta_{\text{K}}^{\text{bg}}$ divided by magnetic field. At T_{CDW} , $\theta_{\text{K}}^{\text{sample}}$ jumps and gradually increases with decreasing temperature, consistent with a first-order transition as previously reported⁴. Moreover, with opposite magnetic field, $\theta_{\text{K}}^{\text{sample}}$ changes its sign to negative. The fact that $\theta_{\text{K}}^{\text{sample}}$ rises concurrently with the CDW transition, and reverses its sign with opposite magnetic field direction is in agreement with the intensity-modulation reversal observed in STM spectroscopy²³ and the AHE⁸, which are interpreted in terms of TRSB and large Berry phase in the CDW state of CsV_3Sb_5 .

Figure 2b shows the temperature dependence of the measured polar Kerr angle θ_{K} . With increasing magnetic field, the magnitude of θ_{K} and the jump $\Delta\theta_{\text{K}}$ at T_{CDW} both increase. In order to obtain the field dependence of the polar Kerr angle, we determine $\Delta\theta_{\text{K}}$ from the difference between two linear fits close to T_{CDW} (the inset of Fig. 2c) and plot it as a function of magnetic field (Fig. 2c). For all three samples, $\Delta\theta_{\text{K}}$ is almost linear in magnetic field in the studied range between -6 T and +10 T, indicating the polar Kerr angle in the CDW state is strongly coupled to the magnetic field. Hence, it is natural to compare $\Delta\theta_{\text{K}}$, proportional to the Hall conductivity at the optical frequency,

with magnetization. For the conventional anomalous Hall conductivity, one expects its magnitude to be proportional to the magnetization. CsV_3Sb_5 is paramagnetic and the magnetization decreases below T_{CDW} due to the decreasing density of states (DOS) (see Supplementary Fig. S1). If $\Delta\theta_{\text{K}}$ originates from the change of magnetization, we would expect also θ_{K} to decrease at T_{CDW} . Our data is opposite to this expectation. Therefore, the change of Pauli paramagnetic spin susceptibility is not the main contribution to the polar Kerr angle jump $\Delta\theta_{\text{K}}$. Instead, we expect a new mechanism to be responsible for the observed Kerr angle data, as we will discuss in the following.

Unusual origin of θ_{K} in CDW. The different origins of the polar Kerr angle and the magnetization in CsV_3Sb_5 is apparent when we compare it with other materials. Figure 3 shows a log-log plot of the magnitude of polar Kerr angle versus magnetization for various materials, including ferro- and ferri-magnets (FM/Ferri) and anti-ferromagnetic (AFM) perovskites with canted spins^{48–52}. Here, the magnetization change associated with the ordering ΔM and the polar Kerr angle $\Delta|\theta_{\text{K}}|$ in the saturated states are plotted (details in the inset of Fig. 3). Despite the relation between θ_{K} and the magnetization can be complicated because θ_{K} is dependent on the light wavelength, the data of FM/Ferri materials fall into the same area, which is distinct from the AFM perovskites. For CsV_3Sb_5 , we plot the change of magnetization and polar Kerr angle jump $\Delta\theta_{\text{K}}$ at T_{CDW} (left inset of Fig. 3) under different magnetic field, where the paramagnetic spins are aligned. Since the magnetization decreases at T_{CDW} , the $\Delta\mu_0 M$ is negative. With increasing magnitude of $\Delta\mu_0 M$, $\Delta\theta_{\text{K}}$ increases. By a linear fitting, we extract the ratio $\Delta|\theta_{\text{K}}|/\Delta\mu_0 M = -1.36 \text{ rad/T}$. The negative sign and the significantly large magnitude of this ratio indicate the polar Kerr angle in CsV_3Sb_5 is decoupled from the paramagnetic spin magnetization. Moreover, we plot $\Delta\theta_{\text{K}}$ and ΔM for the

Kagome magnet Fe_3Sn_2 ^{53,54}, the magnetic Weyl semimetals $\text{Co}_3\text{Sn}_2\text{S}_2$ ^{2,55} and Mn_3Sn ⁵⁶. These materials show similarly large $\Delta|\theta_K|/\Delta\mu_0 M$ ratio, indicating that the polar Kerr effect does not originate from the ordered magnetism. Instead, the origin of such Kerr angle is attributed to the Berry curvature. Interestingly, the CsV_3Sb_5 displays similar magnitude of $\Delta|\theta_K|/\Delta\mu_0 M$ to these materials, but with opposite sign, implying that the polar Kerr effect in the CDW state is probably related to the topologically non-trivial band structure.

Spontaneous TRSB in the CDW phase evidenced by zero-field Kerr effect. At last, we show the presence of non-zero polar Kerr angle at zero field, key feature of spontaneous TRSB and chiral CDW in CsV_3Sb_5 . Figure 4a shows the temperature dependence of θ_K collected at zero field, during both cooling and warming. θ_K fluctuates around zero by $\pm 0.2 \mu\text{rad}$ at high temperature and becomes finite below T_{CDW} , indicating the spontaneous TRSB in the CDW state. We observed that the magnitude and the sign of θ_K vary for each measurement. We repeated this measurement with different optical power and observed similar behaviour. This can be well-explained by random formation of TRSB domains after zero-field-cooling (ZFC). In addition, the magnitude of θ_K tends to grow at a temperature lower than T_{CDW} , probably due to the growth of domain sizes towards low temperature.

In order to obtain clearer TRSB signal and examine the presence of TRSB domains, we performed “field training” experiments to align them. We cooled the sample across T_{CDW} under a perpendicular magnetic field, set the field to zero at low temperature, and then collected data upon zero-field-warming (ZFW). Figure 4b displays multiple sets of data after ± 1 T field training. At

$T > T_{\text{CDW}}$, the data fluctuate around zero. Below T_{CDW} , the positive-field training yields positive θ_{K} and vice versa. Such trends are fully reproducible among all the runs performed. The successful field training implies that the domains are aligned by the magnetic field and that a residual moment persists after removing the field. Comparing Fig. 4a and b, we note that the magnitude of θ_{K} without training is in the range $\pm 1 \mu\text{rad}$, while θ_{K} after field training reaches $\sim 2 \mu\text{rad}$ in some runs at low temperature. This shows how field training effectively aligns TRSB domains. The non-zero θ_{K} and the training effect can be well interpreted as a consequence of TRSB in the CDW state, possibly with a transition temperature $T_{\text{TRSB}} \approx T_{\text{CDW}}$.

Furthermore, we performed field training with magnetic field different from 1T (data in the Supplementary Fig. S6). Figure 4c shows θ_{K} at 50 K plotted against the training field $\mu_0 H_{\text{T}}$. The data show a clear trend that after positive (negative) field training, θ_{K} is positive (negative). The magnitude of the spontaneous polar Kerr angle does not significantly depend on the strength of the training field. This fact may imply that the coercive field of domain alignment across T_{CDW} is much lower than 1 T. We use a step function $\theta_{\text{K}}^{\text{fit}} \text{sgn}(H_{\text{T}})$ to fit the data and get $\theta_{\text{K}}^{\text{fit}} = 0.573 \pm 0.123 \mu\text{rad}$. Data from zero-field training (Fig. 4a), also included in this figure, lie between the two branches of the step function fit.

Discussion

The non-zero θ_{K} at zero field arising below T_{CDW} is a sign of spontaneous TRSB in the CDW state. Since long-range magnetic order has not been detected in CsV_3Sb_5 , the TRSB is not due

to magnetism. Our analysis of the Polar Kerr angle jump $\Delta\theta_K$ under magnetic field displays a behaviour different from the expectation for the conventional anomalous Hall effect originating from the field-induced polarization of paramagnetic spins. Instead, we discuss below that the observed TRSB can be explained in terms of loop-current order in the CDW state.

The CDW in CsV_3Sb_5 is dominated by Fermi-surface nesting characterized by wavevectors connecting the vHSs at the M points of the hexagonal Brillouin zone. The electronic states around the vHS are dominated by vanadium d orbitals. Due to the three sublattices of the Kagome net, the inhomogeneous DOS at E_F promotes nearest-neighbor interaction, thereby resulting in periodic modulation of the bond strength instead of the onsite charge density. This corresponds to a charge bond order (CBO). Further Ginzburg–Landau analysis shows that the three order parameters are imaginary with unequal phases^{32–35}. The imaginary CBO spontaneously induces orbital loop current in the Kagome lattice and hence breaks time-reversal symmetry, as sketched in Fig. 4d. The loop currents (gray arrows) generate opposite chiral flux in hexagons (blue arrow) and triangles (orange arrows). Since both the bond and on-site charge densities are inhomogeneous, an uncompensated net flux appears in each unit cell. Different chiral CDW patterns form domains, and thus, the residue moments over domains are responsible for non-zero polar Kerr angle at zero field (Fig. 4a, b). These domains can be aligned by a moderate magnetic field and result in the observed field-training effect.

In addition, the loop-current order can also explain the Kerr angle jump $\Delta\theta_K$ at T_{CDW} under magnetic field shown in Fig. 2. When a magnetic field is applied, the chiral flux in each hexagon

and triangle tend to be parallel to the external field. However, the energy scale of the CDW transition ($T_{\text{CDW}} \sim 94$ K) is much larger than the magnetic-energy scale of our experiments. Therefore, the total flux, and hence the resulting polar Kerr angle, do not reach saturation and are linearly proportional to the magnetic field.

In AV_3Sb_5 , competing phases have been proposed. The CBO theory with imaginary order parameters suggests rotational-symmetry breaking without translational-symmetry breaking, namely electronic nematicity in the CDW phase³². Such nematicity may be the reason of the bulk two-fold rotational symmetry observed in transport measurements^{27,30}. The CBO theories for the CDW are based on the two-dimensional Kagome lattice. Remarkably, the interlayer charge modulation appears to be important in CsV_3Sb_5 . STM measurement showed that a π -phase shift of the charge modulation intensity across single-unit-cell surface steps has three-dimensional ordering¹⁹. Out-of-plane superlattice peaks have also been observed in X-ray diffraction⁵⁷⁻⁶⁰. Such interlayer coupling may lead to the emergence of multiple sub-phases in the CDW. Indeed, high pressure experiments showed suppression of the CDW phase and unusual two-peak superconducting dome at a moderate pressure^{61,62}. In a μSR study of CsV_3Sb_5 ²⁵, TRSB was observed below 70 K (noticeably lower than $T_{\text{CDW}} \sim 94$ K) along with an additional magnetic transition below 30 K. Other μSR studies on CsV_3Sb_5 and KV_3Sb_5 report that TRSB occurs just below T_{CDW} ^{18,26}. In our data of θ_{K} measured at zero field (Fig. 4a and b), we could not resolve clear transitions between multiple phases, but some datasets exhibit features such as slope or intensity changes at around 60 K and 80 K. These features may hint at competing phases in CDW and call for further investigation.

We notice that optical polarization rotation studies on CsV_3Sb_5 were performed very recently in zero field using 800 nm light and by ordinary polarizer-based optical setups, methodologies different from ours^{63,64}. Both works show the emergence of birefringence and isotropic polarization rotation below T_{CDW} . The former indicates the electronic nematicity and the latter may come from either TRSB or structural chirality. In our study, we use the zero-loop Sagnac interferometer and the detected polar Kerr angle is solely due to TRSB⁴¹. Furthermore, our optical results under magnetic field and field-training effect show that the polar Kerr effect in CsV_3Sb_5 is strongly coupled to magnetic field.

In conclusion, we have studied the TRSB in CDW state of CsV_3Sb_5 via polar Kerr effect. Under magnetic field, the Kerr-angle jump at the CDW transition $\Delta\theta_{\text{K}}$ is proportional to the magnetic field and its sign is field-switchable. Our analysis reveals that $\Delta\theta_{\text{K}}$ increase does not originate from the decreasing magnetization at the CDW transition, indicating that the Kerr effect cannot be ascribed to conventional anomalous Hall effect. At zero field, non-zero θ_{K} arises in the CDW state and can be effectively trained by magnetic field. These results point toward spontaneous TRSB in the CDW states, which can be explained by the loop-current order theory. Our polar Kerr effect results elucidate the central issue of the symmetry breaking in the CDW of CsV_3Sb_5 , motivating further experimental and theoretical research on these Kagome metals. Our study demonstrates that the high-resolution MOKE experiment under low temperature and high magnetic field condition is a powerful tool for exploring non-trivial symmetry breakings, which is crucially important for exploring exotic quantum materials.

Methods

High-quality single crystals of CsV_3Sb_5 were grown by a self-flux method with Cs-Sb binary eutectic mixture ($\text{Cs}_{0.4}\text{Sb}_{0.6}$) as flux²³. The typical lateral size of the obtained crystal is ~ 3 mm. The crystal structure were examined by Laue diffraction at room temperature. The magnetization was measured by a SQUID magnetometer (MPMS, Quantum Design). Polar Kerr angle was measured using an all-fiber zero-loop Sagnac interferometer, constructed based on Ref. 42. We used a broadband light source with wavelength centered at 1550 nm and a line width of 110 nm. The incident light was split into horizontally and vertically polarized components of the polarization-maintaining (PM) fiber, and then phase modulated using an electro-optical modulator (EOM). The modulation frequency was $\omega/2\pi \sim 3.848$ MHz so that the light reflected from the sample has a π phase shift relative to the incident light. The maximum incident optical power is 200 μW and the spot size is ~ 4 μm . The sample surface was cleaved before optical measurements, with typical thickness after cleavage of ~ 100 μm . The low-temperature measurements were performed in a ^4He refrigerator with a base temperature of about 1.9 K. The magnetic field was applied by a 11 T superconducting magnet along the c axis. In the field training measurements, a Hall sensor was used to determine the zero-field with an error within 5 Oe.

Reference

1. Kang, M. *et al.* Dirac fermions and flat bands in the ideal kagome metal FeSn. *Nat. Mater.* **19**, 163–169 (2020).

2. Liu, E. *et al.* Giant anomalous Hall effect in a ferromagnetic kagome-lattice semimetal. *Nat. Phys.* **14**, 1125–1131 (2018).
3. Ortiz, B. R. *et al.* New kagome prototype materials: discovery of KV_3Sb_5 , RbV_3Sb_5 , and CsV_3Sb_5 . *Phys. Rev. Materials* **3**, 094407 (2019).
4. Ortiz, B. R. *et al.* CsV_3Sb_5 : A \mathbb{Z}_2 Topological Kagome Metal with a Superconducting Ground State. *Phys. Rev. Lett.* **125**, 247002 (2020).
5. Ortiz, B. R. *et al.* Superconductivity in the \mathbb{Z}_2 kagome metal KV_3Sb_5 . *Phys. Rev. Materials* **5**, 034801 (2021).
6. Yin, Q. *et al.* Superconductivity and Normal-State Properties of Kagome Metal RbV_3Sb_5 Single Crystals. *Chin. Phys. Lett.* **38**, 037403 (2021).
7. Yang, S.-Y. *et al.* Giant, unconventional anomalous Hall effect in the metallic frustrated magnet candidate, KV_3Sb_5 . *Sci. Adv.* **6**, eabb6003 (2020).
8. Yu, F. H. *et al.* Concurrence of anomalous Hall effect and charge density wave in a superconducting topological kagome metal. *Phys. Rev. B* **104**, L041103 (2021).
9. Kang, M. *et al.* Twofold van Hove singularity and origin of charge order in topological kagome superconductor CsV_3Sb_5 . *Nat. Phys.* **18**, 301–308 (2022).
10. Nakayama, K. *et al.* Multiple energy scales and anisotropic energy gap in the charge-density-wave phase of the kagome superconductor CsV_3Sb_5 . *Phys. Rev. B* **104**, L161112 (2021).

11. Wang, Z. *et al.* Distinctive momentum dependent charge-density-wave gap observed in CsV₃Sb₅ superconductor with topological Kagome lattice. Preprint at <https://arxiv.org/abs/2104.05556> (2021).
12. Luo, H. *et al.* Electronic nature of charge density wave and electron-phonon coupling in kagome superconductor KV₃Sb₅. *Nat. Commun.* **13**, 1–8 (2022).
13. Li, H. *et al.* Observation of Unconventional Charge Density Wave without Acoustic Phonon Anomaly in Kagome Superconductors AV₃Sb₅ (A = Rb, Cs). *Phys. Rev. X* **11**, 031050 (2021).
14. Xie, Y. *et al.* Electron-phonon coupling in the charge density wave state of CsV₃Sb₅. *Phys. Rev. B* **105**, L140501 (2022).
15. Xu, H.-S. *et al.* Multiband Superconductivity with Sign-Preserving Order Parameter in Kagome Superconductor CsV₃Sb₅. *Phys. Rev. Lett.* **127**, 187004 (2021).
16. Zhao, C. C. *et al.* Nodal superconductivity and superconducting domes in the topological Kagome metal CsV₃Sb₅. Preprint at <https://arxiv.org/abs/2102.08356> (2021).
17. Chen, H. *et al.* Roton pair density wave in a strong-coupling kagome superconductor. *Nature* **599**, 222–228 (2021).
18. Mielke, C. *et al.* Time-reversal symmetry-breaking charge order in a kagome superconductor. *Nature* **602**, 245–250 (2022).
19. Liang, Z. *et al.* Three-Dimensional Charge Density Wave and Surface-Dependent Vortex-Core States in a Kagome Superconductor CsV₃Sb₅. *Phys. Rev. X* **11**, 031026 (2021).

20. Ni, S. *et al.* Anisotropic superconducting properties of kagome metal CsV₃Sb₅. *Chin. Phys. Lett.* **38**, 057403 (2021).
21. Ortiz, B. R. *et al.* Fermi surface mapping and the nature of charge-density-wave order in the kagome superconductor CsV₃Sb₅. *Phys. Rev. X* **11**, 041030 (2021).
22. Jiang, Y.-X. *et al.* Unconventional chiral charge order in kagome superconductor KV₃Sb₅. *Nat. Mater.* **20**, 1353–1357 (2021).
23. Wang, Z. *et al.* Electronic nature of chiral charge order in the kagome superconductor CsV₃Sb₅. *Phys. Rev. B* **104**, 075148 (2021).
24. Shumiya, N. *et al.* Intrinsic nature of chiral charge order in the kagome superconductor RbV₃Sb₅. *Phys. Rev. B* **104**, 035131 (2021).
25. Yu, L. *et al.* Evidence of a hidden flux phase in the topological kagome metal CsV₃Sb₅. Preprint at <https://arxiv.org/abs/2107.10714> (2021).
26. Khasanov, R. *et al.* Charge order breaks time-reversal symmetry in CsV₃Sb₅ (2022). Preprint at <https://arxiv.org/abs/2203.12317>.
27. Li, H. *et al.* Rotation symmetry breaking in the normal state of a kagome superconductor KV₃Sb₅. *Nat. Phys.* 1–6 (2022).
28. Ratcliff, N., Hallett, L., Ortiz, B. R., Wilson, S. D. & Harter, J. W. Coherent phonon spectroscopy and interlayer modulation of charge density wave order in the kagome metal CsV₃Sb₅. *Phys. Rev. Materials* **5**, L111801 (2021).

29. Wang, Z. X. *et al.* Unconventional charge density wave and photoinduced lattice symmetry change in the kagome metal CsV_3Sb_5 probed by time-resolved spectroscopy. *Phys. Rev. B* **104**, 165110 (2021).
30. Xiang, Y. *et al.* Twofold symmetry of c-axis resistivity in topological kagome superconductor CsV_3Sb_5 with in-plane rotating magnetic field. *Nat. Commun.* **12**, 1–8 (2021).
31. Zhao, H. *et al.* Cascade of correlated electron states in the kagome superconductor CsV_3Sb_5 . *Nature* **599**, 216–221 (2021).
32. Denner, M. M., Thomale, R. & Neupert, T. Analysis of Charge Order in the Kagome Metal AV_3Sb_5 ($A = \text{K, Rb, Cs}$). *Phys. Rev. Lett.* **127**, 217601 (2021).
33. Feng, X., Zhang, Y., Jiang, K. & Hu, J. Low-energy effective theory and symmetry classification of flux phases on the kagome lattice. *Phys. Rev. B* **104**, 165136 (2021).
34. Feng, X., Jiang, K., Wang, Z. & Hu, J. Chiral flux phase in the Kagome superconductor AV_3Sb_5 . *Sci. Bull.* **66**, 1384–1388 (2021).
35. Lin, Y.-P. & Nandkishore, R. M. Complex charge density waves at Van Hove singularity on hexagonal lattices: Haldane-model phase diagram and potential realization in the kagome metals AV_3Sb_5 ($A=\text{K, Rb, Cs}$). *Phys. Rev. B* **104**, 045122 (2021).
36. Kenney, E. M., Ortiz, B. R., Wang, C., Wilson, S. D. & Graf, M. J. Absence of local moments in the kagome metal KV_3Sb_5 as determined by muon spin spectroscopy. *J. Condens. Matter Phys.* **33**, 235801 (2021).

37. Song, D. *et al.* Orbital ordering and fluctuations in a kagome superconductor CsV₃Sb₅. *Sci. China Phys. Mech. Astron* **65**, 1–8 (2022).
38. Li, H. *et al.* No observation of chiral flux current in the topological kagome metal CsV₃Sb₅. *Phys. Rev. B* **105**, 045102 (2022).
39. Tazai, R., Yamakawa, Y., Onari, S. & Kontani, H. Mechanism of exotic density-wave and beyond-Migdal unconventional superconductivity in kagome metal AV₃Sb₅ (A = K, Rb, Cs). *Sci. Adv.* **8**, eabl4108 (2022).
40. Park, T., Ye, M. & Balents, L. Electronic instabilities of kagome metals: Saddle points and Landau theory. *Phys. Rev. B* **104**, 035142 (2021).
41. Xia, J., Beyersdorf, P. T., Fejer, M. M. & Kapitulnik, A. Modified Sagnac interferometer for high-sensitivity magneto-optic measurements at cryogenic temperatures. *Applied Physics Letters* **89**, 062508 (2006). <https://doi.org/10.1063/1.2336620>.
42. Xia, J., Maeno, Y., Beyersdorf, P. T., Fejer, M. M. & Kapitulnik, A. High Resolution Polar Kerr Effect Measurements of Sr₂RuO₄: Evidence for Broken Time-Reversal Symmetry in the Superconducting State. *Phys. Rev. Lett.* **97**, 167002 (2006).
43. Schemm, E. R., Gannon, W. J., Vishne, C. M., Halperin, W. P. & Kapitulnik, A. Observation of broken time-reversal symmetry in the heavy-fermion superconductor UPt₃. *Science* **345**, 190–193 (2014).
44. Karapetyan, H. *et al.* Evidence of Chiral Order in the Charge-Ordered Phase of Supercon-

- ducting $\text{La}_{1.875}\text{Ba}_{0.125}\text{CuO}_4$ Single Crystals Using Polar Kerr-Effect Measurements. *Phys. Rev. Lett.* **112**, 047003 (2014).
45. Zhou, X. *et al.* Origin of charge density wave in the kagome metal CsV_3Sb_5 as revealed by optical spectroscopy. *Phys. Rev. B* **104**, L041101 (2021).
46. Uykur, E. *et al.* Low-energy optical properties of the nonmagnetic kagome metal CsV_3Sb_5 . *Phys. Rev. B* **104**, 045130 (2021).
47. See Supplemental Material for (i) Magnetic susceptibility of CsV_3Sb_5 . (ii) Polar Kerr angle of Nb and background subtraction for sample #2 of CsV_3Sb_5 . (iii) Polar Kerr angle, second-harmonic signal and their temperature derivative. (iv) Field-training measurements at different magnetic field. (v) The CDW transition in $V_{2\omega}$ (reflectivity) at different light power.
48. Kahn, F. J., Pershan, P. & Remeika, J. Ultraviolet magneto-optical properties of single-crystal orthoferrites, garnets, and other ferric oxide compounds. *Phys. Rev.* **186**, 891 (1969).
49. Nielsen, J. Properties and preparation of magnetic materials for bubble domains. *Metall Mater Trans B* **2**, 625–633 (1971).
50. Buschow, K. v., Van Engen, P. & Jongebreur, R. Magneto-optical properties of metallic ferromagnetic materials. *J. Mag. Mag. Mater.* **38**, 1–22 (1983).
51. Yamamoto, S. & Fujii, T. Magnetic and Magneto-Optical Properties of Sn-Substituted Mn_2Sb Films. *IEEE Translation Journal on Magnetism in Japan* **6**, 862–868 (1991).

52. Zhang, X., Schoenes, J. & Wachter, P. Kerr-effect and dielectric tensor elements of magnetite (Fe_3O_4) between 0.5 and 4.3 eV. *Solid State Commun.* **39**, 189–192 (1981).
53. Wang, Q., Sun, S., Zhang, X., Pang, F. & Lei, H. Anomalous Hall effect in a ferromagnetic Fe_3Sn_2 single crystal with a geometrically frustrated Fe bilayer kagome lattice. *Phys. Rev. B* **94**, 075135 (2016).
54. Schilberth, F. L. *et al.* Magneto-optical detection of topological contributions to the anomalous Hall effect in a kagome ferromagnet. Preprint at <https://arxiv.org/abs/2106.15156> (2022).
55. Okamura, Y. *et al.* Giant magneto-optical responses in magnetic Weyl semimetal $\text{Co}_3\text{Sn}_2\text{S}_2$. *Nat. Commun.* **11**, 1–8 (2020).
56. Higo, T. *et al.* Large magneto-optical Kerr effect and imaging of magnetic octupole domains in an antiferromagnetic metal. *Nat. Photonics* **12**, 73–78 (2018).
57. Chen, Q., Chen, D., Schnelle, W., Felser, C. & Gaulin, B. D. Charge density wave order and fluctuations above T_{CDW} and below superconducting T_c in the kagome metal CsV_3Sb_5 . Preprint at <https://arxiv.org/abs/2203.09386> (2022).
58. Stahl, Q. *et al.* Temperature-driven reorganization of electronic order in CsV_3Sb_5 . Preprint at <https://arxiv.org/abs/2112.02559> (2021).
59. Li, H. *et al.* Spatial symmetry constraint of charge-ordered kagome superconductor CsV_3Sb_5 . Preprint at <https://arxiv.org/abs/2109.03418> (2021).

60. Xiao, Q. *et al.* Coexistence of Multiple Stacking Charge Density Waves in Kagome Superconductor CsV₃Sb₅. Preprint at <https://arxiv.org/abs/2201.05211> (2022).
61. Yu, F. *et al.* Unusual competition of superconductivity and charge-density-wave state in a compressed topological kagome metal. *Nat. Commun.* **12**, 1–6 (2021).
62. Chen, K. Y. *et al.* Double Superconducting Dome and Triple Enhancement of T_c in the Kagome Superconductor CsV₃Sb₅ under High Pressure. *Phys. Rev. Lett.* **126**, 247001 (2021).
63. Wu, Q. *et al.* The large static and pump-probe Kerr effect with two-fold rotation symmetry in Kagome metal CsV₃Sb₅. Preprint at <https://arxiv.org/abs/2110.11306> (2021).
64. Xu, Y. *et al.* Universal three-state nematicity and magneto-optical Kerr effect in the charge density waves in AV₃Sb₅ (A=Cs, Rb, K) (2022). URL <https://arxiv.org/abs/2204.10116>.
65. Momma, K. & Izumi, F. VESTA3 for three-dimensional visualization of crystal, volumetric and morphology data. *J. Appl. Crystallogr.* **44**, 1272–1276 (2011).

Data Availability

All the data that support the findings of this paper are available from the corresponding authors upon reasonable request.

Acknowledgments

We acknowledge M. Cuoco, A. Kapitulnik, Y. Yanase, and J. Goryo, for fruitful discussion. This work was supported by Grant-in-Aids for Scientific Research on Innovative Areas “Quantum Liquid Crystals” (KAKENHI Grant Nos. 20H05158, 22H04473) from the Japan Society for the Promotion of Science (JSPS), a Grant-in-Aid for JSPS Fellows (KAKENHI Grant No. 20F20020) from JSPS, Grant-in-Aids for Scientific Research (KAKENHI Grant Nos. 17H06136, 22H01168) from JSPS, by Core-to-Core Program (No. JPJSCCA20170002) from JSPS, by a research support funding from The Kyoto University Foundation, and by ISHIZUE 2020 of Kyoto University Research Development Program. G. Mattoni acknowledges the support from the Dutch Research Council (NWO) through Rubicon Grant No. 019.183EN.031. The work at Beijing was supported by the Natural Science Foundation of China (Grant No. 92065109), the National Key R&D Program of China (Grant No. 2020YFA0308800), the Beijing Natural Science Foundation (Grant No. Z210006). Z. Wang thanks the Analysis&Testing Center at BIT for assistance in facility support. The work at UCI is funded by the Gordon and Betty Moore Foundation through Grant GBMF10276 to Jing Xia.

Author contributions

This study was designed by S. Yonezawa and Y. Maeno. Y. Hu and S. Yamane performed polar Kerr effect measurements and analyses, with assistance from G. Mattoni, K. Yada, J. Wang, C. Farhang, J. Xia, S. Yonezawa, and Y. Maeno. Y. Hu, S. Yamane, and K. Obata performed the

magnetization measurements. K. Obata took Laue diffraction images. Z. Wang, Y. Li, and Y. Yao grew single crystalline samples and characterized them. The manuscript was mainly written by Y. Hu and S. Yonezawa, based on discussion among all authors.

Competing financial interests

All authors declare there is no competing interests regarding this work.

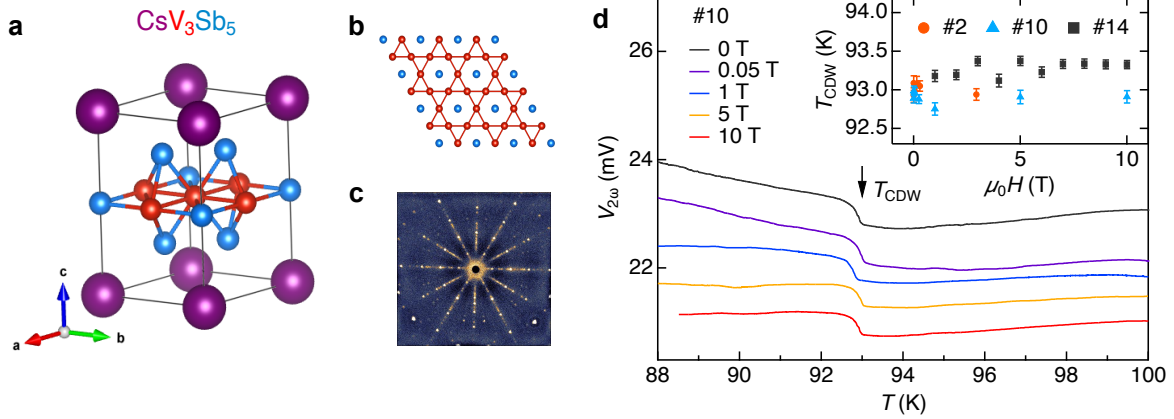


Figure 1: Crystal structure of CsV_3Sb_5 and CDW transition detected by reflectivity. **a.** Room-temperature crystal structure of CsV_3Sb_5 . **b.** Kagome net formed by V atoms (red spheres). Sb atoms (blue spheres) are located at the hexagonal center. The crystal structure is illustrated by using the software VESTA⁶⁵. **c.** Laue diffraction image taken on sample #14 along the [001] direction. **d.** Temperature dependence of the second-harmonic signal $V_{2\omega}$, which is proportional to the sample reflectivity, near the CDW transition measured on sample #10 at different magnetic fields. The arrow indicates the CDW transition. The inset shows the magnetic-field dependence of the transition temperature T_{CDW} of samples #2, #10 and #14. T_{CDW} is determined by the peak in the temperature derivative of $V_{2\omega}$. These data show that T_{CDW} is nearly the same for all three samples and independent of H .

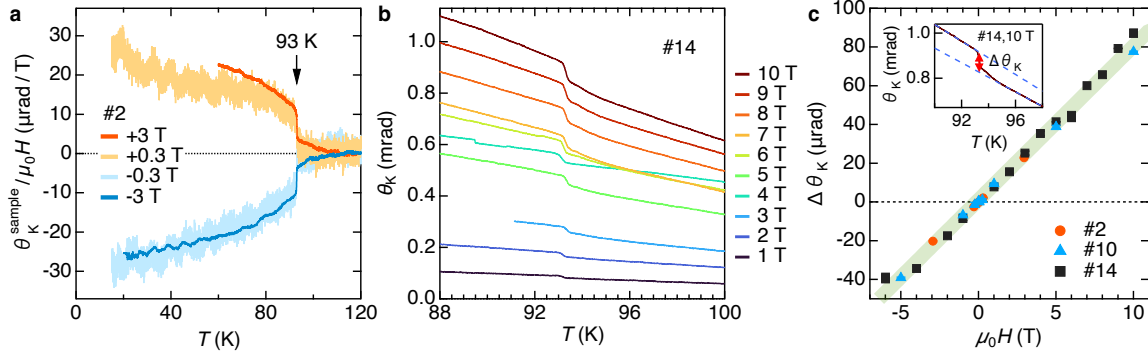


Figure 2: Temperature and magnetic field dependence of the polar Kerr angle of CsV₃Sb₅. **a.** Temperature dependence of the background-subtracted polar Kerr angle $\theta_K^{\text{sample}} = \theta_K - \theta_K^{\text{bg}}$ divided by magnetic field for sample #2. The polar Kerr angle θ_K of a Nb metal sheet obtained by a separated measurement was used as the background θ_K^{bg} (see Supplementary Fig. S2). **b.** Temperature dependence of θ_K for #14 measured from 1 T (bottom curve) to 10 T (top curve) upon cooling. **c.** Polar Kerr angle jump $\Delta\theta_K$ at T_{CDW} as a function of magnetic field for three samples. $\Delta\theta_K$ is determined by the difference at T_{CDW} between the linear fits below and above T_{CDW} , as exemplified in the inset. The shaded region indicates a line with slope $\Delta\theta_K / \mu_0 H \sim 8.0 \mu\text{rad}/\text{T}$ deduced from all the data.

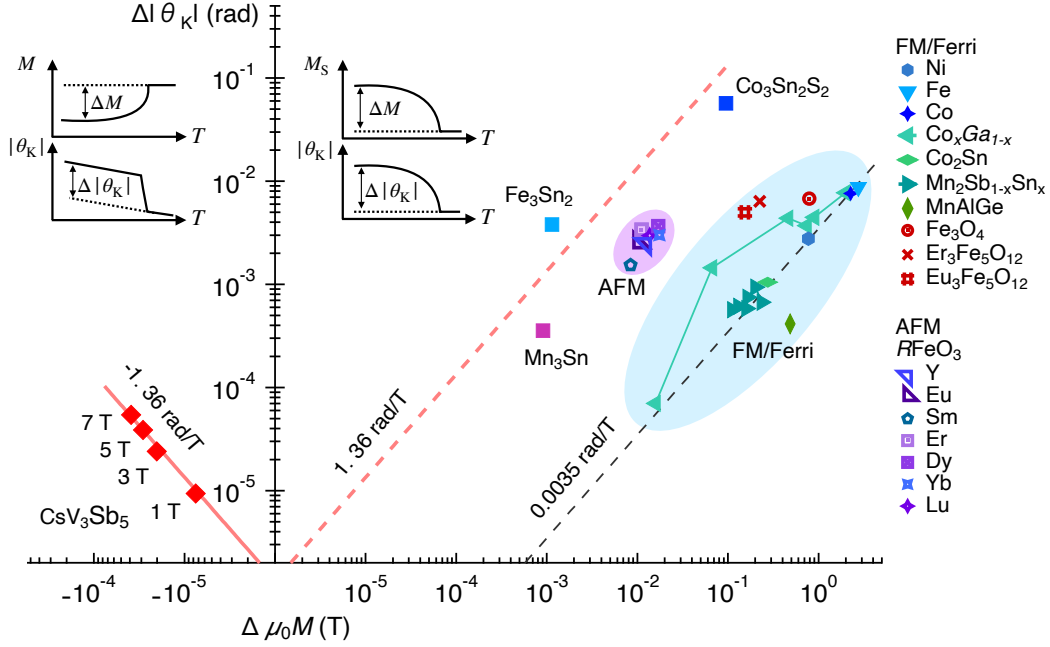


Figure 3: Relationship between magnetization and the polar Kerr effect for various materials, including CsV_3Sb_5 . In the right side of the graph, polar Kerr angle versus magnetization observed in the ordered state is plotted in log-log scale for various ferromagnetic (FM), ferrimagnetic (Ferri) and anti-ferromagnetic (AFM) materials, as well as the Kagome magnet Fe_3Sn_2 and magnetic Weyl semimetals $\text{Co}_3\text{Sn}_2\text{S}_2$ and Mn_3Sn ^{2,48–56}. Here, the horizontal axis indicates the change of the saturated magnetization due to the ordering ΔM , and the vertical axis is the change of the Kerr angle in the ordered state, as illustrated in the right inset. The gray dashed line indicates an empirical linear relationship with slope 0.0035 rad/T for FM/Ferri materials⁵⁶. For CsV_3Sb_5 , the estimated polar Kerr angle jump $\Delta\theta_K$ and change of magnetization at T_{CDW} at 1 to 7 T obtained for sample #10 are plotted. The definitions of plotted values are schematically shown in the left inset. The red solid line is the linear fit to the CsV_3Sb_5 data with slope -1.36 rad/T, and the red dashed line is a line with positive slope for comparison purposes.

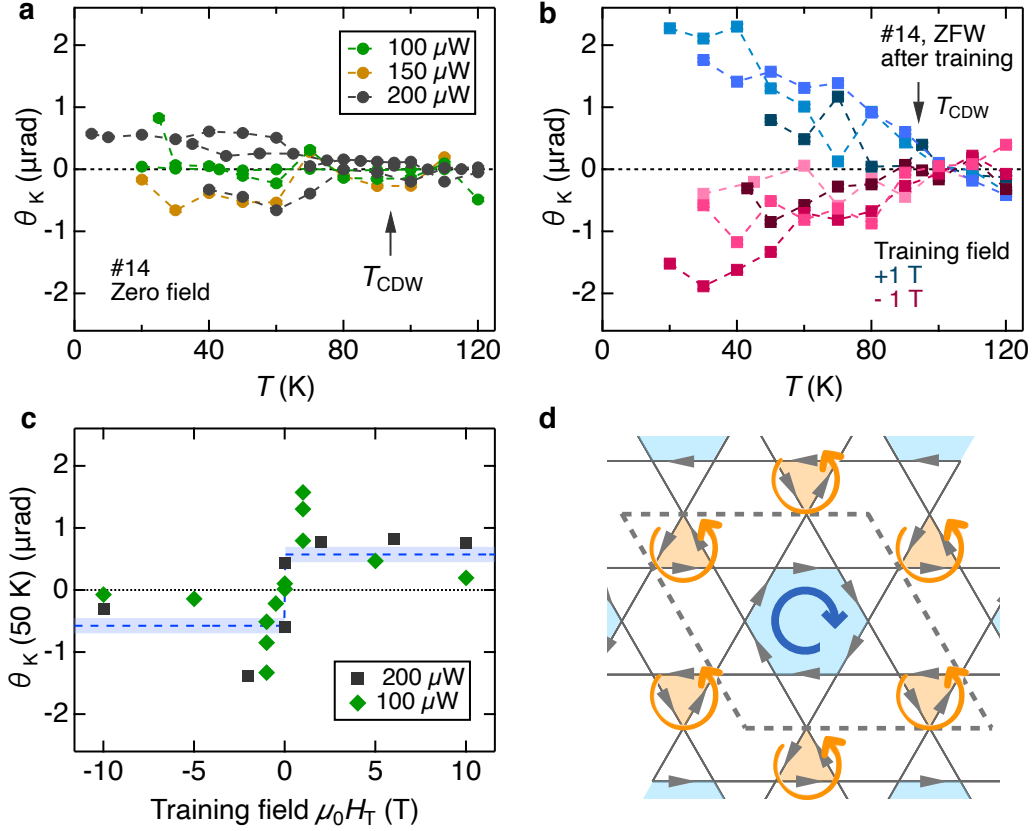


Figure 4: Polar Kerr effect at zero field and field training effect to probe spontaneous TRSB in CsV_3Sb_5 . **a.** Temperature dependence of the polar Kerr angle θ_K measured at zero field. The data are obtained at different incident optical powers of $100 \mu\text{W}$, $150 \mu\text{W}$ and $200 \mu\text{W}$. The arrow indicates $T_{\text{CDW}} \sim 94 \text{ K}$. **b.** Temperature dependence of θ_K measured during zero-field-warming (ZFW) after cooling from above T_{CDW} with a training field of $\pm 1 \text{ T}$. The incident optical power is $\sim 100 \mu\text{W}$. The arrow indicates T_{CDW} . The data show systematic positive (negative) trend with positive (negative) training field. For (a) and (b), each data point is obtained by averaging the signal for 2 hours. The error bar is the standard error and is within the size of the markers. **c.** θ_K at 50 K versus training field for measurements with $\sim 100 \mu\text{W}$ and $\sim 200 \mu\text{W}$. The blue dashed line is the fitting by a step-function $\theta_K^{\text{fit}} \text{sgn}(H_T)$, the shaded area indicating the error bar. The fitted magnitude of Kerr angle θ_K^{fit} is $0.573 \pm 0.123 \mu\text{rad}$. **d.** Schematic of the real-space loop-current pattern in the Kagome lattice³⁵. The grey arrows indicate the orbital current direction. The associated chiral flux is indicated by the clockwise and counter-clockwise arrows. Within the unit cell in the CDW state (dashed lines), there are two triangles and one hexagon with opposite chiral flux. Their incomplete compensation, predicted by theories, would result in non-zero spontaneous Kerr effect.

Supplemental Information for “Time-reversal symmetry breaking in charge density wave of CsV_3Sb_5 detected by polar Kerr effect”

Yajian Hu^{1*}, Soichiro Yamane¹, Giordano Mattoni^{1,2}, Kanae Yada¹, Keito Obata¹, Yongkai Li^{3,4,5}, Yugui Yao^{3,4}, Zhiwei Wang^{3,4,5}, Jingyuan Wang⁶, Camron Farhang⁶, Jing Xia⁶, Yoshiteru Maeno^{1,2}, Shingo Yonezawa^{1†}

¹*Department of Physics, Graduate School of Science, Kyoto University, Kyoto 606-8502, Japan*

²*Toyota Riken-Kyoto University Research Center (TRiKUC), Kyoto University, Kyoto 606-8501, Japan*

³*Centre for Quantum Physics, Key Laboratory of Advanced Optoelectronic Quantum Architecture and Measurement (MOE), School of Physics, Beijing Institute of Technology, Beijing 100081, P. R. China*

⁴*Beijing Key Lab of Nanophotonics and Ultrafine Optoelectronic Systems, Beijing Institute of Technology, Beijing 100081, P. R. China*

⁵*Material Science Center, Yangtze Delta Region Academy of Beijing Institute of Technology, Jiaxing 314011, P. R. China*

⁶*Department of Physics and Astronomy, University of California, Irvine, California 92697, USA*

*e-mail: hu.yajian.78e@st.kyoto-u.ac.jp †e-mail: yonezawa@scphys.kyoto-u.ac.jp

Dated: August 17, 2022

Magnetic susceptibility of CsV₃Sb₅

Figure S1a shows the temperature dependence of the magnetic susceptibility $\chi = M/H$ measured under in-plane field of 7 T for both zero-field-cooling (ZFC) and field-cooling (FC) conditions. It shows paramagnetic behaviour at high temperature. The magnetic susceptibility χ shows a sharp drop at ~ 94 K, corresponding to the charge density wave (CDW) transition. At T_{CDW} , gaps open on several parts of the Fermi surface and hence the density of states (DOS) at the Fermi level drops, leading to the decrease of the Pauli susceptibility. The ZFC and FC data almost overlap with each other. Figure S1b is the magnetic susceptibility measured at 5 Oe below 5 K. A sharp superconducting transition is observed at $T_c^{\text{onset}} \sim 2.9$ K. These data are consistent with previous studies^{1,2} and indicative of high quality of the sample.

Background subtraction for CsV₃Sb₅ sample #2

In our experiment, the Faraday effect of lens and fiber becomes significant under magnetic field and contribute to the measured signal. In order to quantify the polar Kerr effect from the CDW transition in CsV₃Sb₅, we used a Nb metal sheet, which is non-magnetic above $T_c \sim 9.2$ K, to measure the background contribution. This measurement was done under experimental conditions similar to the measurements of sample #2. Figure S2a shows the measured θ_K for Nb at 0.3 T. We fit the data with a polynomial function to capture the temperature dependence and the resulted curve is denoted as θ_K^{Nb} . The background signal at a different θ_K^{Nb} magnetic field H is defined as $\theta_K^{\text{bg}} = \theta_K^{\text{Nb}} \times \frac{\mu_0 H}{0.3} \times C$, where C is a constant determined by matching θ_K^{bg} with the data of CsV₃Sb₅ above

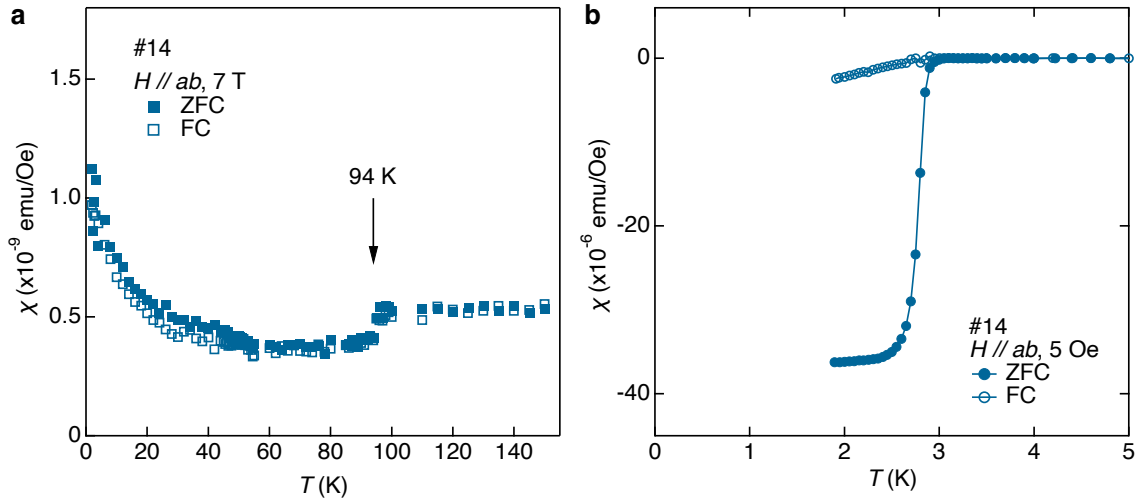


Figure S1: Temperature dependence of the magnetic susceptibility of CsV_3Sb_5 of sample #14. **a.** Temperature dependence of the magnetic susceptibility χ measured at 7 T. The magnetic field is in the ab plane. The closed markers represent data collected at warming after zero-field-cooling (ZFC), while the open markers represent data measured during field-cooling (FC). The arrow indicates $T_{\text{CDW}} \sim 94$ K. **b.** Temperature dependence of χ measured at 5 Oe parallel to the ab plane below 5 K, showing a sharp superconducting transition. The solid markers represent data collected at warming after zero-field-cooling (ZFC). The open markers represent data measured during field-cooling (FC).

T_{CDW} . We found that the constant C deviates from 1 typically by about 20%. This may be due to the slight changes in the modulation frequencies and the positions of the lens and fiber in the magnetic field. Figures S2b and c show θ_K of CsV_3Sb_5 measured at 0.3 T and 3 T together with the background signal θ_K^{bg} . By subtracting θ_K^{bg} from θ_K , we obtain the background-subtracted polar Kerr angle $\theta_K^{\text{sample}} = \theta_K - \theta_K^{\text{bg}}$, as shown in Fig. S2d and Fig. 2a in the main text. Note that in Fig. S2c, the measured θ_K and θ_K^{bg} start to deviate below ~ 100 K and make θ_K^{sample} at 3 T above T_{CDW} increase. This is probably because the θ_K of Nb was measured at 0.3 T and may have slightly different temperature dependence from θ_K at 3 T. Nevertheless, the small upturn in the θ_K^{sample} at 3 T does not affect our observation that the polar Kerr angle from the sample changes at T_{CDW} and this change can be switched by magnetic field.

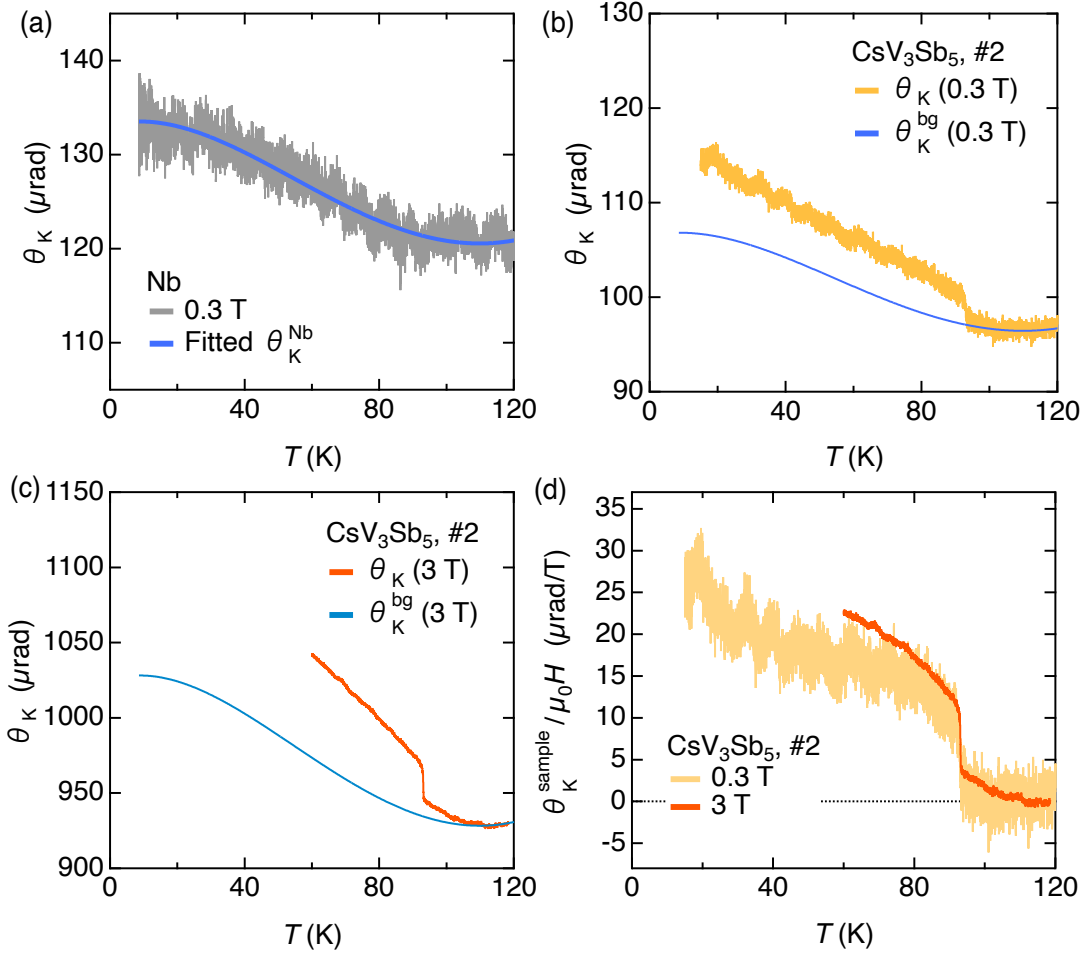


Figure S2: Examples of background subtraction to produce the data in Fig 2a of the main text, for sample #2. **a.** Temperature dependence of the polar Kerr angle θ_K of a Nb sheet measured at 0.3 T. The data is fitted by a polynomial function, as shown by the blue curve, θ_K^{Nb} . **b.** Temperature dependence of θ_K of CsV_3Sb_5 measured at 0.3 T. The background signal is $\theta_K^{\text{bg}}(0.3 \text{ T}) = \theta_K^{\text{Nb}} \times 0.8$. **c.** Temperature dependence of θ_K of CsV_3Sb_5 measured at 3 T. The background signal is $\theta_K^{\text{bg}}(3 \text{ T}) = \theta_K^{\text{Nb}} \times 10 \times 0.77$. **d.** Temperature dependence of the polar Kerr angle after background subtraction ($\theta_K - \theta_K^{\text{bg}}$) divided by magnetic field, the same as data shown in Fig. 2a of the main text.

Polar Kerr angle, second-harmonic signal and their temperature derivatives

In this section, we present the raw data used to extract the transition temperature T_{CDW} and polar Kerr angle jump $\Delta\theta_{\text{K}}$, presented in the inset of Fig. 1b and Fig. 2c of the main text. Among the three measured samples, the data are consistent.

Figure S3a shows the temperature derivative of the second-harmonic signal $V_{2\omega}$ (proportional to the sample reflectivity) near the CDW transition of #14. The data are collected from 1 T to 10 T. The sharp peaks around 93 K indicate the CDW transition. T_{CDW} is determined by the temperature where $|dV_{2\omega}/dT|$ peaks.

Figure S3b shows θ_{K} measured under negative magnetic field. At T_{CDW} , the polar Kerr angle shows a drop, which is symmetric to the data shown in Fig. 2b measured under positive field.

In the temperature dependence of θ_{K} , there is a tiny upturn (downturn) under positive (negative) magnetic field at ~ 95 K (Fig. 2b of the main text), implying an onset behaviour. We calculated the temperature derivative of the polar Kerr angle $|d\theta_{\text{K}}/dT|$, as shown in Fig. S3c, in order to investigate this behaviour more in detail. The sharp peaks indicate the jumps in θ_{K} at the CDW transition. Above 5 T, $|d\theta_{\text{K}}/dT|$ shows a broad hump above T_{CDW} . This feature may be attributed to multiple domains within the light spot area, which is not surprising for a CDW system exhibiting a first-order phase transition. Moreover, the hump becomes larger at higher magnetic field. If the hump above T_{CDW} comes from another domain which contribute only a tiny portion to the total signal, when the magnetic field is higher, θ_{K} is enhanced almost linearly and the hump

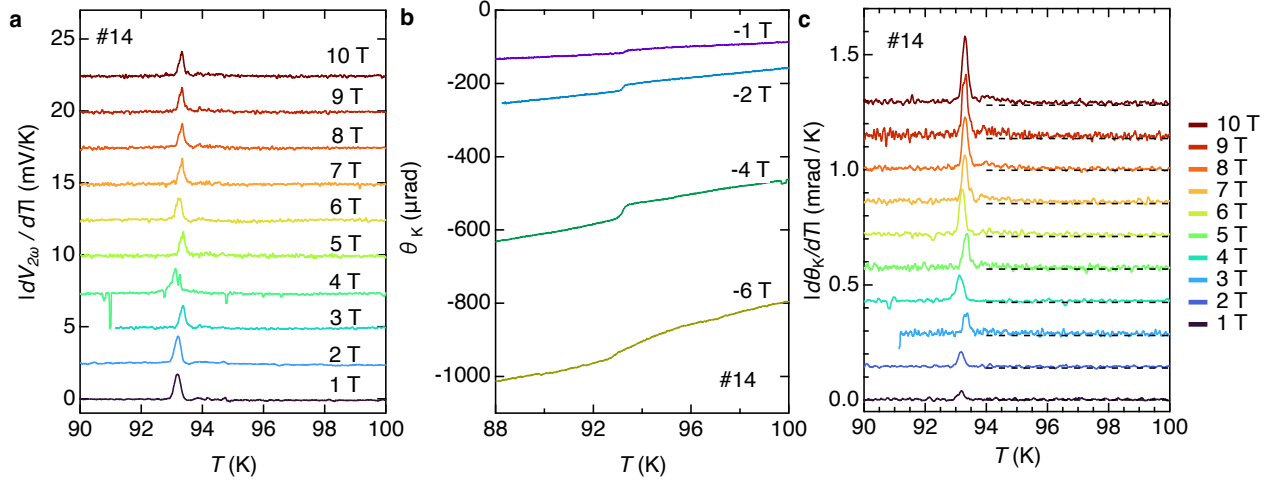


Figure S3: Temperature derivative of $V_{2\omega}$, θ_K , and its temperature derivative of sample #14. a. Temperature dependence of the temperature derivative of $V_{2\omega}$ under magnetic field. The data are vertically offset for clarity. **b.** Temperature dependence of θ_K measured under negative magnetic field. **c.** Temperature dependence of $|d\theta_K/dT|$ under magnetic field. The data are offset for clarity. The dashed lines indicate the constant $|d\theta_K/dT|$ above T_{CDW} .

part becomes more visible.

Figure S4 shows the data of sample #10. The temperature derivative of the second-harmonic signal $|dV_{2\omega}/dT|$ shows a peak around 93 K, as shown in Fig. S4a. The data are used to obtain T_{CDW} up to 10 T (Fig. 1b). Figure S4b shows the temperature dependence of θ_K . For opposite magnetic fields, both the θ_K and the jump at T_{CDW} are flipped. The tiny kinks around 90 K in the ± 5 T data are due to drastic temperature change. Figure S5 shows the similar data measured on sample #2. The $|dV_{2\omega}/dT|$ shows peaks at T_{CDW} and the θ_K can be flipped by opposite magnetic fields.

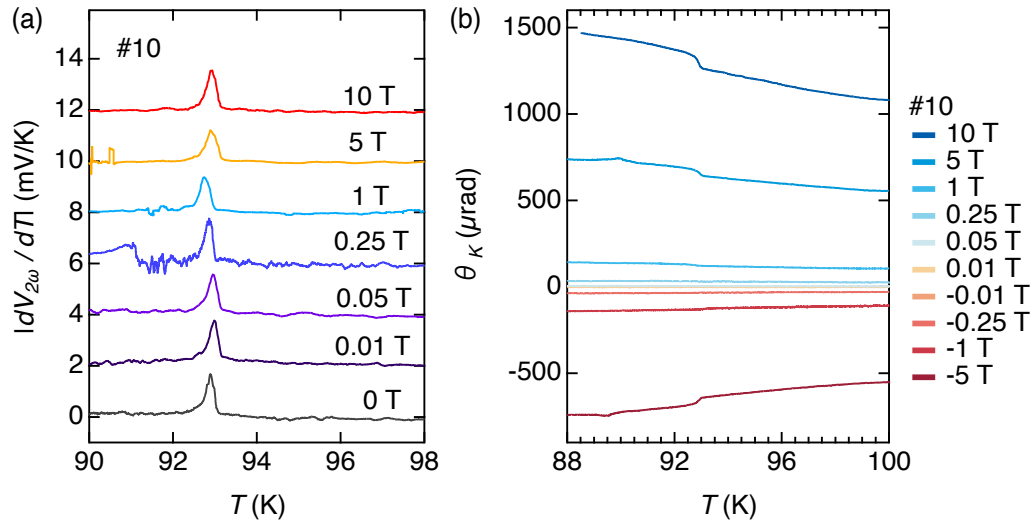


Figure S4: Temperature derivative of $V_{2\omega}$ and θ_K of sample #10. **a.** Temperature dependence of the temperature derivative of $V_{2\omega}$ under magnetic field. The data are vertically offset for clarity. **b.** Temperature dependence of θ_K measured under magnetic field.

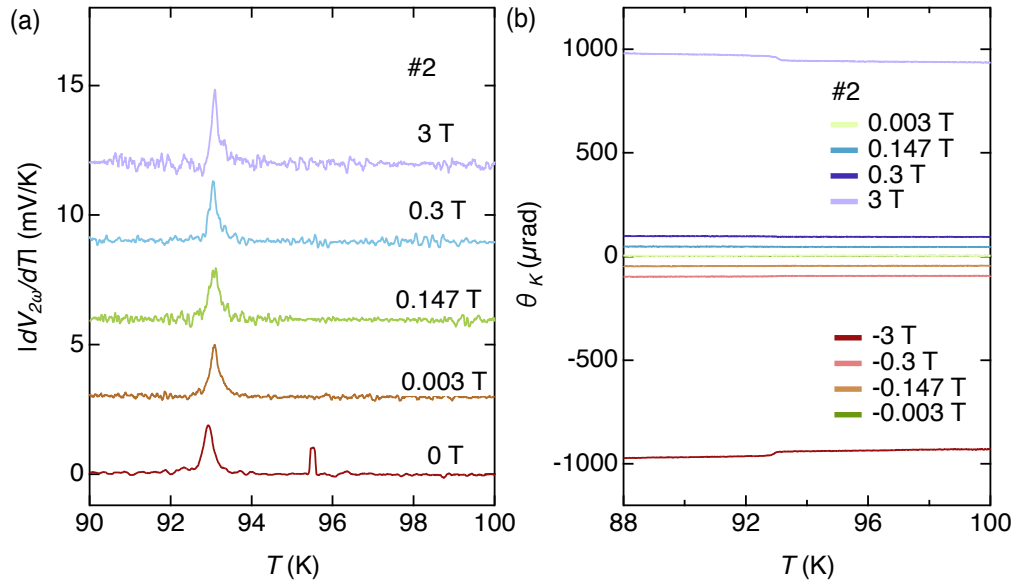


Figure S5: Temperature derivative of $V_{2\omega}$ and θ_K of sample #2. **a.** Temperature dependence of the temperature derivative of $V_{2\omega}$ under magnetic field. The data are vertically offset for clarity. **b.** Temperature dependence of θ_K measured under magnetic field.

Field-training measurements at different magnetic fields

Here, we present θ_K after different field-training, from which we extract the data in Fig. 4c of the main text. Figure S6 compares the temperature dependence of θ_K measured at zero-field-warming (ZFW) after field-cooling from above T_{CDW} with incident light power $\sim 200 \mu\text{W}$ and $\sim 100 \mu\text{W}$. All the data reproduce the field-training effect, showing a positive (negative) trend for positive (negative) training field.

For $200 \mu\text{W}$ measurements (Fig. S6a), the $\pm 2 \text{ T}$ and 6 T data points are obtained by averaging the signal for 1 hour, while the $\pm 10 \text{ T}$ data are obtained by 2-hour averaging. For $100 \mu\text{W}$ measurements (Fig. S6b), the data points are obtained by averaging the signal for 2 hours. We note that the fluctuation of $100 \mu\text{W}$ data is smaller than that of $200 \mu\text{W}$. This result contradicts the naive expectations and may be attributed to the domain effect and the heating effect. The light of smaller power effectively has smaller spot size. When the size of the light spot is comparable to the domain size, the spot of smaller power covers less domains and may reduce fluctuation. In addition, with smaller light power, the heating on sample surface is lower and may reduce thermal noise.

In Fig. S7, we present the temperature dependence of $V_{2\omega}$ (proportional to reflectivity) near T_{CDW} measured at 4 T with different light power. The data are normalized by $V_{2\omega}$ at 95 K . With decreasing power from $200 \mu\text{W}$ to $19 \mu\text{W}$, the CDW transition temperature T_{CDW} increases by around 1 K . Moreover, with smaller power, the transition tends to show two steps with a sharp jump at lower temperature and a broader jump at higher temperature. This feature is consistent with

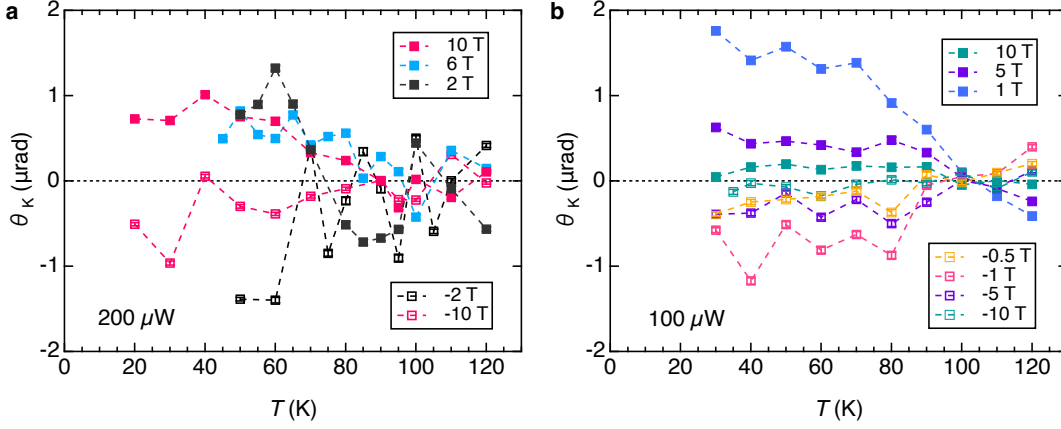


Figure S6: Temperature dependence of θ_K measured at zero-field-warming after field-training. **a.** θ_K measured with light power $\sim 200 \mu\text{W}$. **b.** θ_K measured with light power $\sim 100 \mu\text{W}$. A set of ± 1 T field training data shown in the main text is also plotted. The data are collected on sample #14.

the domain effect and the change of effective size of the light spot. For a smaller power (smaller effective spot size), a fewer number of domains are measured and the contribution from minor domains (with higher T_{CDW}) becomes more visible. Comparing the sharp jump at the transition, the difference of T_{CDW} between $200 \mu\text{W}$ and $100 \mu\text{W}$ is ~ 0.2 K. Thus, the heating effect should not be severe in our measurements.

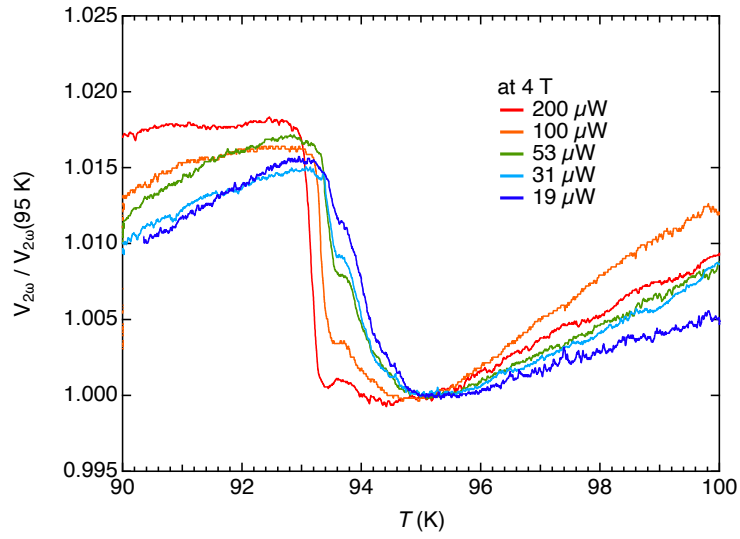


Figure S7: Temperature dependence of $V_{2\omega}$ near T_{CDW} with different light power. The data are collected on sample #14 at 4 T. $V_{2\omega}$ is normalized to $V_{2\omega}(95 \text{ K})$ in order to compare the transition temperature.

Reference

1. Ortiz, B. R. *et al.* New kagome prototype materials: discovery of KV_3Sb_5 , RbV_3Sb_5 , and CsV_3Sb_5 . *Phys. Rev. Materials* **3**, 094407 (2019).
2. Ortiz, B. R. *et al.* CsV_3Sb_5 : A \mathbb{Z}_2 Topological Kagome Metal with a Superconducting Ground State. *Phys. Rev. Lett.* **125**, 247002 (2020).